Applied Catalysis B: Environmental 196 (2016) 1–15

Contents lists available at ScienceDirect

Applied Catalysis B: Environmental

journal homepage: www.elsevier.com/locate/apcatb

Facile preparation of novel graphene oxide-modified $Ag_2O/Ag_3VO_4/AgVO_3$ composites with high photocatalytic activities under visible light irradiation

Rong Ran [a,b], Xiangchao Meng [a,b], Zisheng Zhang [a,b,*]

[a] Department of Chemical and Biological Engineering, University of Ottawa, Ottawa, Ontario, K1N 6N5, Canada
[b] Centre for Catalysis Research and Innovation, University of Ottawa, Ottawa, Ontario, K1N 6N5, Canada

ARTICLE INFO

Article history:
Received 9 October 2015
Received in revised form 3 May 2016
Accepted 6 May 2016
Available online 10 May 2016

Keywords:
Multi-phase $Ag_2O/Ag_3VO_4/AgVO_3$
Multi-morphology photocatalyst
Graphene oxide
Visible light photocatalysis

ABSTRACT

A series of graphene oxide-modified, multi-phase $Ag_2O/Ag_3VO_4/AgVO_3$ composites were synthesized via simple procedures at room temperature. Compared to those of pure $Ag_2O/Ag_3VO_4/AgVO_3$, these GO-modified composites exhibited enhanced activities during photocatalytic degradation of rhodamine B and methyl orange under visible light illumination. A study of the effect of graphene oxide (GO) addition on photocatalytic performance indicated that 1.2 wt% GO was the optimum quantity. The increased photocatalytic activities of as-prepared GO-modified composites may be attributed to the large surface area possessed by GO as well as its interactions with other species in the multi-phase $Ag_2O/Ag_3VO_4/AgVO_3$ composites during photocatalytic reactions under visible light illumination. From the enhancement in photocatalytic activity, it may be inferred that GO could improve the adsorption and absorption capabilities of the $Ag_2O/Ag_3VO_4/AgVO_3$ composites and promote the separation of electron-hole (e-h) pairs during photocatalytic reactions compared to those of composites without GO addition. Moreover, GO as a modifier was able to partially protect silver species composites from photocorrosion. A possible mechanism was proposed for the photocatalytic degradation of organic dyes on the surface of GO-modified $Ag_2O/Ag_3VO_4/AgVO_3$.

1. Introduction

Strategies have been investigated for the synthesis of metal oxide photocatalysts with low band gap energies and increased visible-light-driven photocatalytic activities, primarily to be used in the degradation of organic pollutants [1–3]. Using single-phase photocatalysts, it has been reported that the increase in the recombination rate of photogenerated e-h pairs may be attributed to defects in the grain boundaries of photocatalysts. These defects serve as recombination centers to impede the separation of charged species [1,4,5]. Heterojunction photocatalysts are capable of increasing their photocatalytic activities, attributed to both the matched band potentials amongst each phase as well as the high transfer efficiency of charges at the interface [6].

Silver-based photocatalysts, for instance, Ag_2O [9], Ag_2CO_3 [10], Ag_3PO_4 [7], and Ag_3VO_4 [11] show high photocatalytic activities with respect to the degradation of organic pollutants under visible light irradiation (VLI). However, the instability of silver species photocatalysts manifests in the form of photocorrosion in the composites during photocatalytic performance under VLI. When Ag+ were reduced to metallic silver (Ag^0), the active sites of photocatalysts would be blocked by the Ag^0, so as to decrease their photocatalytic activities [8]. It suggest the sacrificial agents or modifiers are needed to prevent the silver ions being reduced by photogenerated electrons when silver-based photocatalysts being applied [7]. For instance, Yu et al. reported on preparation of Ag_2O [12], AgI [13] and TiO_2 [14] modified Ag_2CO_3 heterostructures. The stability of Ag_2CO_3 during the photocatalytic process was greatly improved and the photocatalytic activity in degradation of organic pollutants was also enhanced when these modifiers were added [15].

Graphene oxide (GO) is one of the highly oxidative forms of graphene, attracting a considerable amount of attention in the field of waste-water treatment [16,17]. Functionalized, GO-modified photocatalysts have attracted considerable research interests due to their large specific surface areas, strong adsorption capabilities and their abundance of reactive sites used for surface modification

* Corresponding author at: Department of Chemical and Biological Engineering, University of Ottawa, Ottawa, Ontario, K1N 6N5, Canada.
E-mail address: zzhang@uOttawa.ca (Z. Zhang).

http://dx.doi.org/10.1016/j.apcatb.2016.05.012
0926-3373/

Fig. 1. Schematics of the route used in the synthesis of GO-modified multi-phase $Ag_2O/Ag_3VO_4/AgVO_3$ powders.

reactions [18]. The remarkable characteristics of GO not only allow functional groups such as those containing oxygen to effectively photodegrade pollutants, but also allow GO to serve as a modifier, providing possible protection to photocatalysts from photocorrosion during visible-light-driven photocatalysis [16,17].

The implementation of GO with silver species composites has been rightfully increasing in popularity recently. Li et al. have reported that a GO/Ag_2CO_3 composite boasted an enhanced visible light adsorption of MO, as well as a higher photocatalytic activity and stability towards the degradation of MO under visible light irradiation, which was attributed to the synergistic effects of GO and Ag_2CO_3 [19]. Furthermore, it was found that GO prevents Ag^+ from reducing to Ag^0 by accepting photogenerated electrons. Other reports have also shown that compounds such as Ag_2O [20], Ag_3PO_4 [21,22], Ag_2CO_3 [23,24] and Ag/AgX (X = Br, Cl) [25,26], amongst others, have demonstrated improved photocatalytic activities towards the degradation of organic pollutants under VLI. This suggests that functionalized GO-modified silver species composites facilitate visible-light-driven photocatalytic activity in several aspects. Firstly, the combination of GO with these composites improves both the efficiency of transferring charges (both electrons and holes) at the interface of photocatalysts, as well as increases the mobilities of photogenerated electrons and holes in photocatalysts [22,27]. This results in suppression of the recombination of e-h pairs in photocatalysts due to the high electrical conductivity of GO. Secondly, the adsorption of organic dyes is favoured at the interface of photocatalysts due to the strong π-π interactions between GO and organic molecules [28]. Thirdly, GO was incorporated with two or more particles resulting in the modification of photocatalyst morphologies [25,29]. The fabrication of functionalized GO-modified silver species photocatalysts therefore shows a strong potential for highly active, visible-light-driven photocatalytic performances in the field of water decontamination.

In this study, a facile fabrication process is proposed to obtain visible-light-driven, multi-phase, heterogeneous $Ag_2O/Ag_3VO_4/AgVO_3$ photocatalysts modified by various quantities of GO, synthesized via simple chemical procedures at room temperature (RT). These prepared photocatalyst composites were then studied with regards to the photodegradation of model organic pollutants, i.e. rhodamine B (RhB) and methyl orange (MO), and then compared to the photodegradation performed by pure $Ag_2O/Ag_3VO_4/AgVO_3$. A possible mechanism for the photocatalytic degradation of organic dyes is discussed. The accelerated visible-light-driven photocatalytic activity towards the degradation of organic dyes may be attributed to the synergistic effects between the three photosensitive phases and the characteristics of GO. Quite possibly, this could be the first report regarding the novel multi-phase heterogeneous GO-modified $Ag_2O/Ag_3VO_4/AgVO_3$ photocatalysts with highly active photocatalytic performances under VLI.

2. Experimental

2.1. Synthesis

GO-modified multi-phase $Ag_2O/Ag_3VO_4/AgVO_3$ photocatalysts were prepared via simple procedures using potassium metavanadate (KVO_3), silver nitrate and GO as starting materials. KVO_3 was synthesized via calcination, in which 0.38 g of K_2CO_3 (Fisher Scientific, Certified ACS) and 0.50 g of V_2O_5 (ACROS Organics, 99.6%) were dissolved in 35 mL of deionized water (DW) under vigorous magnetic stirring. The resultant solution was poured into an evaporation dish and dried overnight at 50 °C in an oven (Sheldon Manufacturing, Inc. Model No: 1350 GM). The dry sample was ground in an agate mortar and calcined in air at 457 °C (730 K) for 5 h, yielding a pink KVO_3 powder. The molar ratio of silver to vanadium (Ag to V) used was 4:1.

Fig. 1 shows a schematic of the preparation of the GO-modified multi-phase $Ag_2O/Ag_3VO_4/AgVO_3$ powders. A quantity of 15 mL of as-prepared 0.1 M KVO_3 aqueous solution was obtained after treatment in a water bath at 60 °C for 3 min. Next, 60 mL of dispersion mixture containing 0.1 M $AgNO_3$ (Fisher Scientific, Certified ACS) and 4 mg mL^{-1} GO (dispersion in H_2O, Sigma-Aldrich) was prepared under vigorous magnetic stirring for 1.5 h. Subsequently, the dispersion mixture containing $AgNO_3$ and GO was added dropwise to the KVO_3 solution and allowed to react under continuous stirring for 30 min to obtain a yellow slurry. The pH of the resulting slurry was then adjusted by adding 1 M KOH solution until a final pH of 7 was reached, verified by a pH meter (Fisher Scientific, accumet basic, AB 15 pH meter), resulting in a dark green slurry. The slurry was then maintained at room temperature overnight after 1 h of magnetic stirring. The resulting solid was collected by centrifugation, washed four times with DW, and then dried in air at room temperature overnight.

In the experiment, six GO-modified samples were prepared with initial graphene oxide quantities of 0.5 wt%, 0.8 wt%, 1.0 wt%, 1.2 wt%, 1.5 wt% and 2.0 wt%, where the weight percentage is designated as the weight ratio of GO to silver composites. For comparison, pure silver composite was also synthesized via the previously described methods, excluding the addition of graphene oxide.

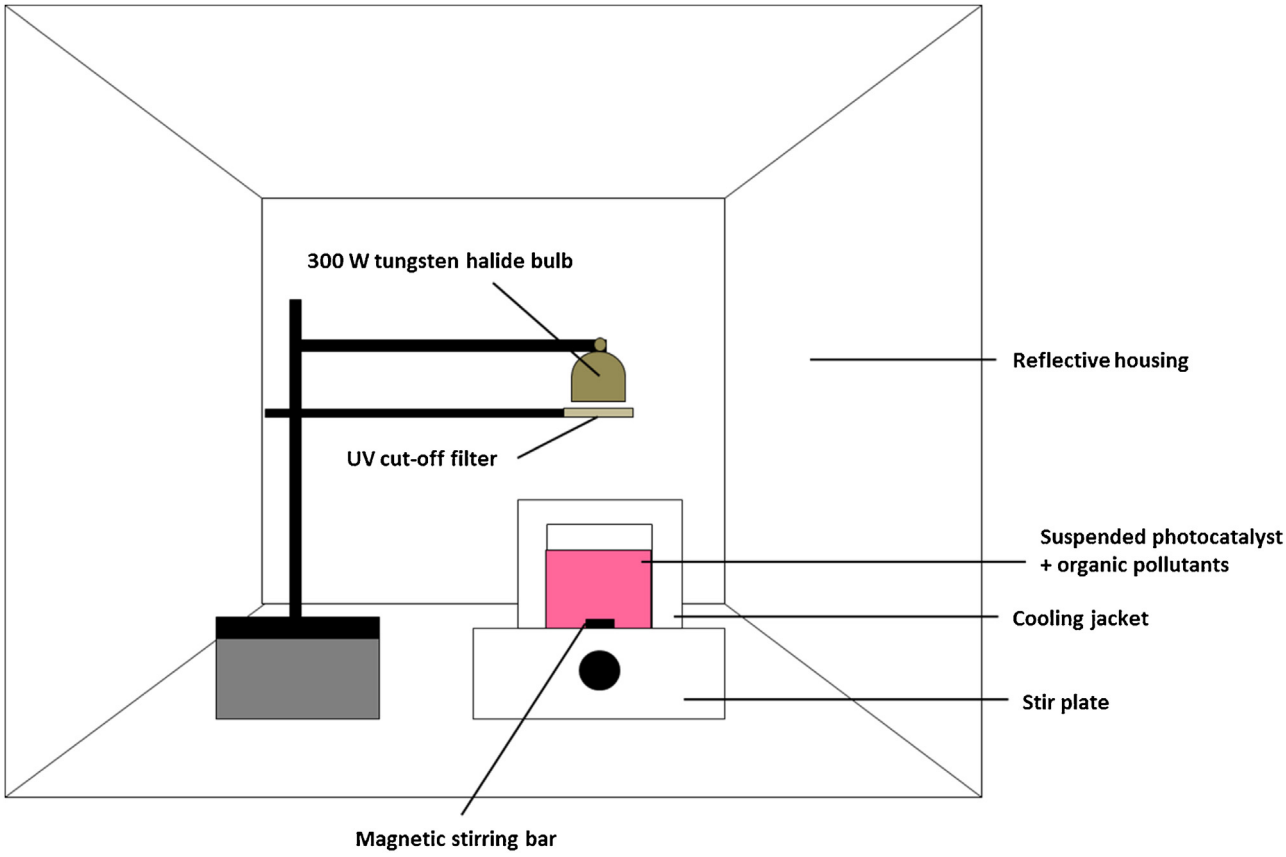

Fig. 2. Experimental set up for catalyst activity test.

2.2. Characterization

Powder X-ray diffraction (XRD) measurements were carried out in Bragg-Brentano geometry on a Rigaku Ultima IV apparatus with Cu Kα1 (λ = 0.15418 nm) radiation, operating at 40 kV and 44 mA, using a scanning range of 2θ from 15° to 70°. The morphologies of the prepared samples were obtained by scanning electron microscopy (SEM) (JEOL JSM-7500F field emission SEM), scanning transmission electron microscopy (STEM) (JEOL JSM-7500F field emission SEM), and transmission electron microscopy (TEM) [JEOL JEM-2100F field emission TEM operated at 120 kV; FEI (formerly Phillips) Tecnai G2 F20 field emission TEM at an acceleration voltage of 200 kV]. STEM-Energy-dispersive X-ray spectroscopy (STEM-EDS) was performed using an energy dispersive X-ray detector (JSM-7500F SEM). X-ray photoelectron spectroscopy (XPS) was conducted on a Kratos Analytical Axis Ultra DLD instrument with mono-chromated Al X-rays at 140 W. The powder UV–vis diffuse reflectance spectra (DRS) were recorded on a Thermo Evolution 300 UV/Vis spectrophotometer equipped with a Praying Mantis diffuse reflectance accessory, and the spectra were collected at a scan rate of 240 nm min^{-1}. UV/Vis spectra of RhB samples were obtained using a Biochrom Ultrospec 60 UV/Vis spectrophotometer.

2.3. Photocatalytic activity

2.3.1. Photodegradation of RhB

Photocatalytic performance was quantified by the decomposition of RhB (Sigma-Aldrich) as a model organic pollutant under VLI. A device in the photocatalytic activity test is shown in Fig. 2. A slurry reactor was placed in a reflective housing unit to prevent external radiation from entering the reactor, as well as to prevent internal radiation from exiting the system.

A 300-W ELH tungsten halide bulb (Ushio) was used as a light source with a 410 nm cut-off filter (Kenko Zeta, λ > 410 nm, transmittance >90%) to provide VLI. The light source was placed at a distance of 15 cm from the top of the slurry. The corresponding irradiation was measured using a quantum meter (Biospherical QSL-2100; 400 nm < λ < 700 nm), and was found to be approximately 10.9×10^{-3} Einstein m^{-2} s^{-1}. Cooling was provided by an external cooling jacket (Fisher Scientific K3170001000, Beaker Jacketed, 1000 mL), and the temperature of the reaction was controlled to 20 ± 2 °C.

Before illumination, 0.15 g of photocatalysts were dispersed into 150 mL of 15 mg L^{-1} RhB solution and was allowed to reach adsorption-desorption equilibrium under continuous magnetic stirring at 280 rpm for 40 min in the absence of light. Irradiation was then provided for 45 min for each photocatalytic degradation trial. A sample was taken every 5 min and separated by centrifugation at 10^4 rpm for 3 min in an accuSpin Micro 17 (Fisher Scientific) microcentrifuge to remove the suspended catalyst particles. The supernatant fluid was analyzed by monitoring the peak absorbance (λ = 554 nm for RhB) using a Genesys 10-UV spectrophotometer (Geneq Inc.). A standard curve for RhB was prepared and the concentration determined by the measured absorbance and the Beer-Lambert Law. UV/Vis analysis of RhB samples was accomplished with a Biochrom Ultrospec 60 UV/Vis spectrophotometer.

Quenching tests were performed through the addition of appropriate reactive species scavengers. A quantity of 0.015 g of benzoquinone (BQ) (reagent-grade ≥ 98%, Sigma Aldrich) was used to trap superoxide radicals ($O^{2-\bullet}$), 0.15 g of ammonium oxalate (AO) (ACS, Sigma-Aldrich) was used as the hole scavenger, and 3 mL of *tert*-butyl alcohol (TBA) (ACS, Sigma-Aldrich) was used to trap hydroxyl radicals ($^{\bullet}OH$).

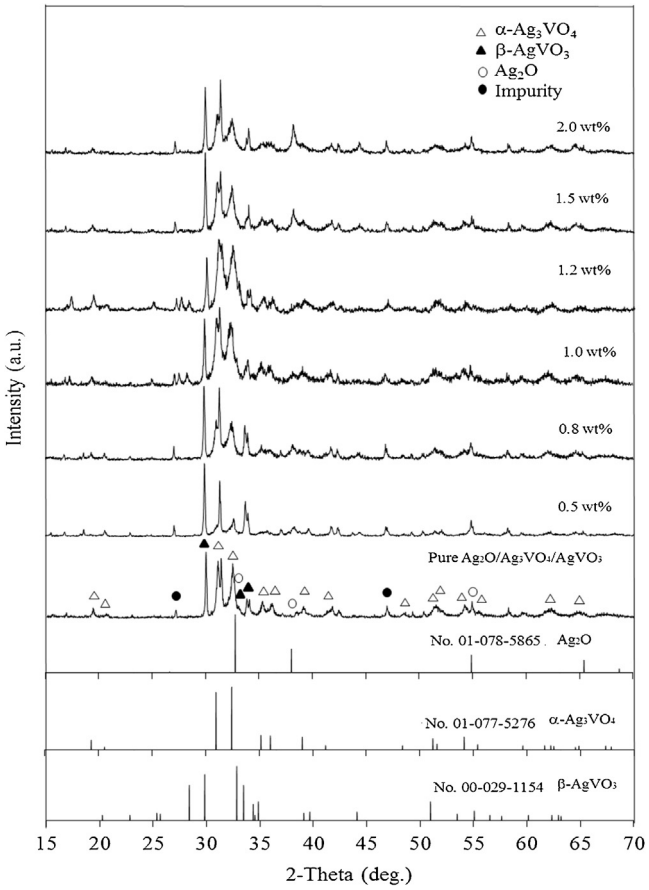

Fig. 3. XRD patterns of fresh, multi-phase pure $Ag_2O/Ag_3VO_4/AgVO_3$ and GO-modified $Ag_2O/Ag_3VO_4/AgVO_3$ composites with various quantities of GO.

2.3.2. Photodegradation of MO

The photocatalytic degradation of MO (Fisher Scientific) induced by the GO-modified multi-phase $Ag_2O/Ag_3VO_4/AgVO_3$ photocatalysts synthesized via KVO_3 was also investigated. The same parameters and methodologies that were seen in the RhB photocatalysis studies were applied, where the spectrophotometric analysis was performed at a peak absorbance, corresponding to a wavelength of 463 nm. Quenching tests were also performed to investigate the roles of reactive species in photocatalysis, which was achieved through the addition of the same reactive species scavengers which were used in the RhB photocatalysis studies.

3. Results and discussion

3.1. XRD analysis

Fig. 3 shows the XRD patterns of the fresh multi-phase and pure composites, as well as those modified by graphene oxide, i.e. GO-modified $Ag_2O/Ag_3VO_4/AgVO_3$, in the presence of various quantities of GO obtained via simple chemical reactions.

As seen in Fig. 3, the patterns of multi-phase, pure and GO-modified heterogeneous photocatalysts exhibited crystal structures including monoclinic α-Ag_3VO_4 phases (JCPDS Card No. 01-077-5276), monoclinic β-$AgVO_3$ phases (JCPDS Card No. 00-029-1154), and cubic silver oxide phases (JCPDS Card No. 01-078-5865) respectively. The diffraction peaks observed from the pure sample indicate that α-Ag_3VO_4 is the dominant phase in the heterogeneous composite due to a pH of 7. Major reflections for α-Ag_3VO_4 which occurred at 30.96° (1 1 2) and 32.42° (−3 1 2) agreed well with the results reported by Pan et al. [30]. Apart from α-Ag_3VO_4, β-$AgVO_3$ and Ag_2O are the other two main phases presented in the heterogeneous composites, and the major reflections for β-$AgVO_3$ and Ag_2O were identified at 29.84° (5 0 1), 32.85° (−4 1 1), as well as 33.48° (−1 1 2) and 32.78° (1 1), 38.03° (2 0 0), as well as 54.88° (2 2 0) respectively. In addition, two unknown diffraction peaks which emerged at 27.02° and 46.82° were identified as impurities according to the observed patterns.

Compared to the multi-phase pure heterogeneous composite, no significant differences in the diffraction peaks were found in the GO-modified multi-phase heterogeneous photocatalysts, suggesting that the introduction of GO had little impact on the crystal structure of multi-phase $Ag_2O/Ag_3VO_4/AgVO_3$ [31], with the exception of the sample containing 0.5 wt% GO. The intensities of major peaks for α-Ag_3VO_4 at 30.96° and 32.42° decreased in the GO-modified heterogeneous sample with 0.5 wt% GO, suggesting that the amount of GO had some influence on the formation of crystallinity in the crystal structure of α-Ag_3VO_4 during the preparation process. Furthermore, the amount of Ag_2O particles was found to increase proportionally to the amount of GO in as-prepared composites, and the maximum amount of Ag_2O was observed in the 2.0 wt% GO-modified sample shown in Fig. 3. However, the major peaks for β-$AgVO_3$ at 29.84°, 32.85° and 33.48° showed little change, which indicates that the amount of GO had little impact on the formation of crystallinity in β-$AgVO_3$ during synthesis. Moreover, no obvious GO peaks were detected, which can most likely be ascribed to the low quantities of GO in the samples. The diffraction peak corresponding to GO was barely visible in the XRD pattern when hybridized with inorganic components due to the low diffraction intensity of GO [26].

3.2. SEM analysis

The microstructures and morphologies present in the prepared fresh, multi-phase pure $Ag_2O/Ag_3VO_4/AgVO_3$ composite, as well as composites with various quantities of GO were investigated by SEM, the results of which are shown in Fig. 4a-g. From these figures, it is clear that the as-obtained samples with different quantities of GO were observed to be multi-scale particles with multi-morphological features. In Fig. 4a, multi-morphological structures composed of 2 μm-wide chunks and 3 μm-long dendritic-like plates can be seen, both of which were decorated with flake-like and nanoscale granular particles. The nanoscale granular particles were identified as Ag_2O nanoparticles (NPs) according to the XRD results, the results of which were corroborated with studies from relevant literature sources [9,32]. As such, multi-morphological structures could increase the surface areas of as-prepared composites by increasing their adsorption efficiencies to promote solid-liquid heterogeneous photocatalytic reactions [8,33,34].

The morphologies of the as-prepared samples varied slightly at different quantities of GO. A comparison of Fig. 4b, c and d shows obvious aggregations of those nanoparticles found in the as-obtained samples in the additions of 0.5 wt%, 0.8 wt% and 1.0 wt% GO respectively. This indicates that the GO weight ratio may influence the dispersion of the multi-morphological structures during synthesis, possibly due to the electrostatic interactions between GO sheets and the multi-scale particles present in the system [16,25]. In particular, many distinct monoclinic crystal structures which were identified as α-Ag_3VO_4 crystal structures emerged in the GO-modified samples, highlighted in the insets of Fig. 4b-i. This agrees with the results obtained from the XRD patterns and in reports from other scholars [35,36]. In addition, the lamella sheet in the system was observed and identified as GO, which is highlighted in the inset of Fig. 4b-ii. It can be seen that the lamella sheet was covered and filled with numerous nanoscale granular particles on the top, indicating that GO sheets as substrates offer large surface areas to distribute nanoparticles rather than to agglomerate them

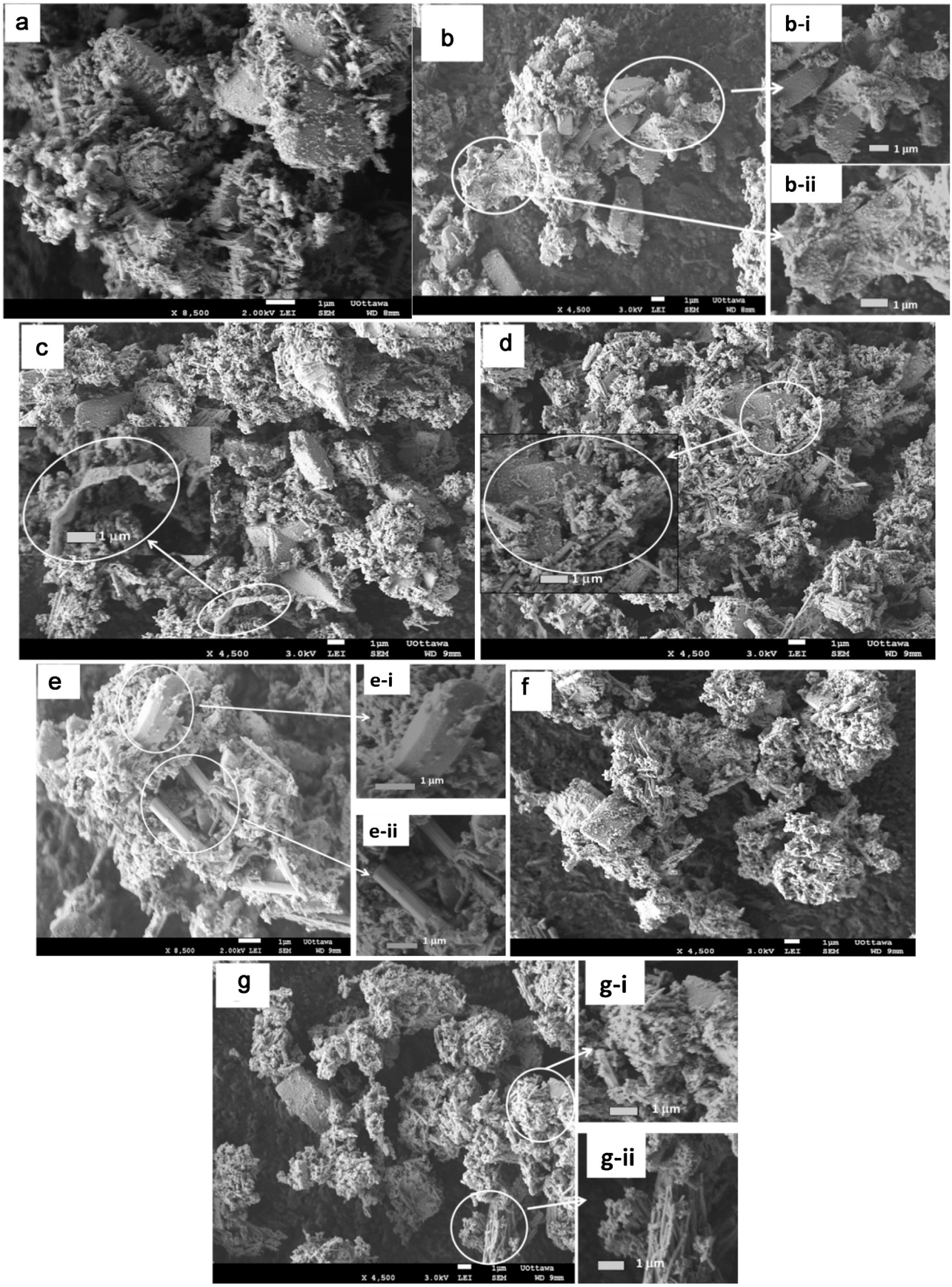

Fig. 4. SEM images of fresh, multi-phase pure and GO-modified $Ag_2O/Ag_3VO_4/AgVO_3$ composites with various quantities of GO. (a): pure composite; (b): 0.5 wt%; (c): 0.8 wt%; (d): 1.0 wt%; (e): 1.2 wt%; (f): 1.5 wt%; (g): 2.0 wt%.

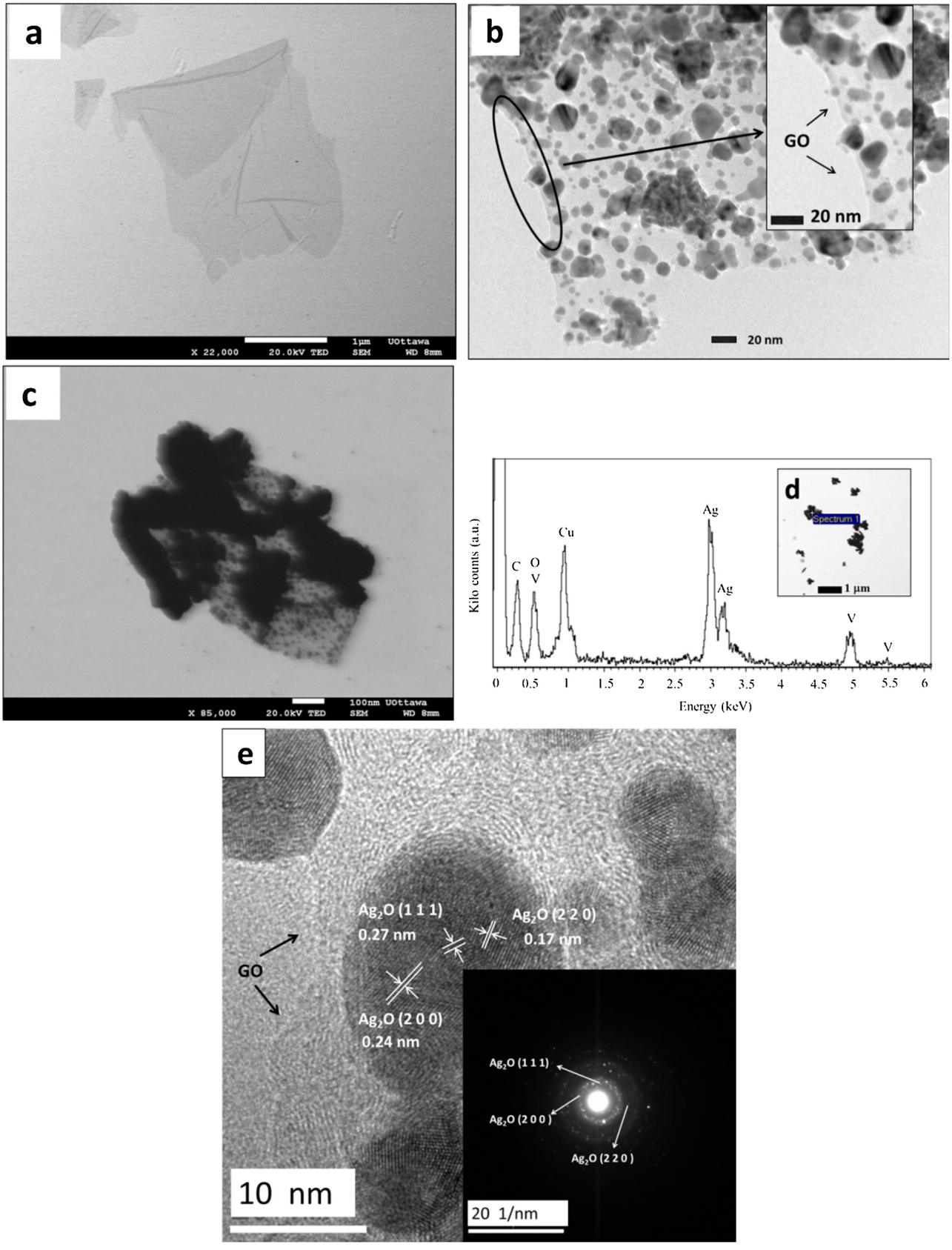

Fig. 5. (a): STEM of GO sheets. (b and c): TEM and STEM images of the fresh 1.2 wt% GO-modified $Ag_2O/Ag_3VO_4/AgVO_3$ composite. (d): Enlarged image of an arbitrarily selected point in (c) and its EDS data. (e): high-resolution TEM of 1.2 wt% GO-modified $Ag_2O/Ag_3VO_4/AgVO_3$ composite and SAED patterns (inset).

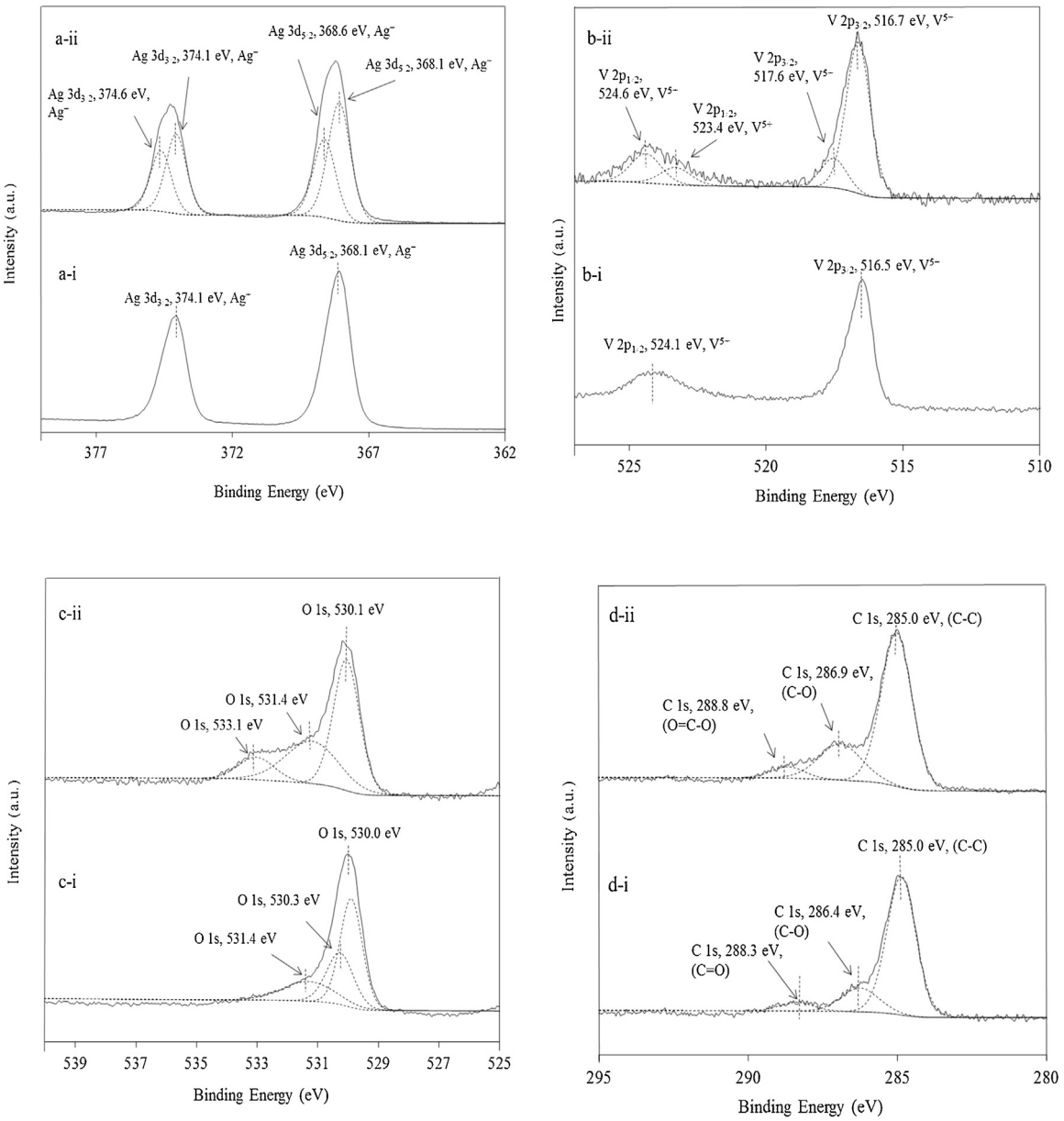

Fig. 6. High-resolution XPS spectra of fresh, multi-phase pure (a-i, b-i, c-i and d-i) and 1.2 wt% GO-modified $Ag_2O/Ag_3VO_4/AgVO_3$ (a-ii, b-ii, c-ii and d-ii) composites. (a-i and a-ii): Ag 3d; (b-i and b-ii): V 2p; (c-i and c-ii): O 1s; (d-i and d-ii): C 1s.

together, resulting in the increased specific surface areas of the composites [18]. As such, the same morphology of GO was found and demonstrated in the inset of Fig. 4c. Moreover, from Fig. 4d, the elongated, cylindrical-like structures were observed and identified as β-$AgVO_3$ crystals, which agrees well with XRD results and existing sources of literature [30,37]. This indicates that the morphological features of the as-prepared samples were influenced by the addition of GO.

In a comparison of Fig. 4e, f and g, the apparent octagonal crystal structures were observed and highlighted in the insets of Fig. 4e-i and e-ii. Most notably, the 1.2 wt% GO sample was observed with three different morphologies: prismatic monoclinic crystals, elongated prismatic crystals, and nanoscale granular particles. This suggests that the yielded composites possess high crystallinities that demonstrate multi-morphological features after simple chemical procedures with a composition of 1.2 wt% GO. Nevertheless, many agglomerated structures are exhibited in Fig. 4f and g, which display prismatic monoclinic crystal structures encrusted by elongated, cylindrical-like structures and nanoscale particles rather than yielding bare crystal structures. This suggests that larger surface areas on large, prismatic monoclinic crystals were formed using GO as the carrier to distribute small crystal structures and nanoparticles. In addition, some elongated nanofibers were shown to have emerged, highlighted in the inset of Fig. 4g-ii, and were identified as β-$AgVO_3$. Therefore, the multi-morphological features of the prepared samples may be attributed to the effects of the cooperation of GO with multi-phase composites, resulting in the increased specific surface areas of large crystal structures and giving rise to the high efficiencies of adsorption processes. This could eventually facilitate the exhibition of high photocatalytic degradation efficiencies with regards to organic dyes [8,23].

3.3. STEM-EDS and TEM analyses

In order to further investigate the multiple morphologies and the detailed structures of GO-modified $Ag_2O/Ag_3VO_4/AgVO_3$ com-

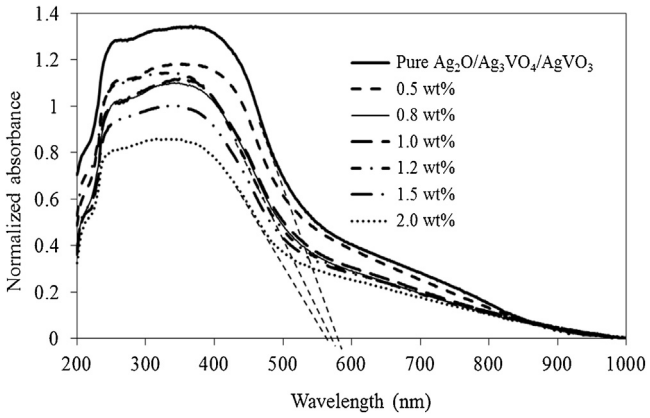

Fig. 7. UV–vis DRS spectra of fresh samples with different quantities of GO.

posites, STEM-EDS and TEM were employed to provide deeper analyses of the prepared samples. Results are shown in Fig. 5a-e.

As shown in Fig. 5a, GO sheets exhibited super-thin layers with microscale ranges, which agrees well with the images observed in Fig. 4b-ii and c. This indicates that GO increased the specific surface areas of composites, resulting in strong adsorption capabilities [18]. From the TEM image shown in Fig. 5b, the noticeable distribution of multi-phase $Ag_2O/Ag_3VO_4/AgVO_3$ composites with the modification of 1.2 wt% GO was observed, indicating that using GO sheets as the reticulate substrate resulted in an even distribution of nanoscale particles over large surface areas, thus preventing agglomeration. In addition, the distinct distribution of multi-morphological $Ag_2O/Ag_3VO_4/AgVO_3$ composites in various size ranges is exhibited in the STEM image found in Fig. 5c and provides supporting evidence for the analyses performed in the previous SEM section. Furthermore, regarding the results shown in Fig. 5d, EDS data indicated that the elemental composition of the as-obtained 1.2 wt% GO-modified sample was primarily silver, vanadium, carbon and oxygen. It should be noted that the copper (Cu) peak occurred as a result of the sputter coating.

In Fig. 5e, a high-resolution TEM image of the 1.2 wt% GO-modified $Ag_2O/Ag_3VO_4/AgVO_3$ photocatalyst exhibits lattice fringes of 0.27 nm, 0.24 nm and 0.17 nm, which correspond to the (1 1 1), (2 0 0) and (2 2 0) interlayer spacings (*d-spacings*) of Ag_2O, respectively. In addition, the selected area electron diffraction (SAED) patterns shown in the inset of Fig. 5e further confirmed the crystal structure of Ag_2O present in the multi-phase crystalline structure of the $Ag_2O/Ag_3VO_4/AgVO_3$ photocatalyst. The rings were ascribed to diffraction from the (1 1 1), (2 0 0) and (2 2 0) reflections of the Ag_2O phase (JCPDS Card No. 01-078-5865), based on the calculated *d-spacings* of 2.73 Å, 2.36 Å, and 1.67 Å, respectively.

3.4. XPS analysis

The chemical and electronic states of the as-synthesized, fresh, multi-phase, pure samples, as well as that of the multi-phase 1.2 wt% GO-modified $Ag_2O/Ag_3VO_4/AgVO_3$ composite were implemented via XPS analysis, the results of which are shown in Fig. 6a-i, a-ii, b-i and b-ii, c-i and c-ii, as well as Fig. 6d-i and d-ii for Ag 3d, V 2p, O 1s and C 1s states, respectively. The obtained binding energies from XPS analysis were calibrated by referencing C 1s to 285 eV.

In a comparison of the high-resolution spectra of pure samples and the 1.2 wt% GO-modified sample observed in Fig. 6a-i, b-i, c-i, and d-i as well as Fig. 6a-ii, b-ii, c-ii, and d-ii, the addition of GO slightly impacted the chemical and electronic states of the components in the GO-modified sample. Two individual peaks observed centered at 368.1 eV and 374.1 eV in Fig. 6a-i were assigned to the spin-orbit splitting characteristics of Ag $3d_{5/2}$ and Ag $3d_{3/2}$, respectively. However, the slight deconvolution spectra of Ag 3d (dashed lines in Fig. 6a-ii) which occurred in the presence of the 1.2 wt% GO-modified sample were centered at binding energies of 368.1 eV and 368.6 eV (ascribed to Ag $3d_{5/2}$), as well as binding energies of 374.1 eV and 374.6 eV (ascribed to Ag $3d_{3/2}$). All of the Ag 3d peaks corresponded to Ag^+ both in pure and 1.2 wt% GO-modified samples, which agrees with results reported in literature sources [25,38,39]. A similar situation occurred with the peaks of V 2p. The observed peaks shown in Fig. 6b-i were ascribed to V $2p_{3/2}$ at a binding energy of 516.5 eV, and V $2p_{1/2}$ centered at a binding energy of 524.1 eV. V 2p spectra shown in Fig. 6b-ii were deconvoluted into two sets of peaks (dashed lines in Fig. 6b-ii) centered at 516.7 eV and 517.6 eV as well as at 523.4 eV and 524.6 eV. All such

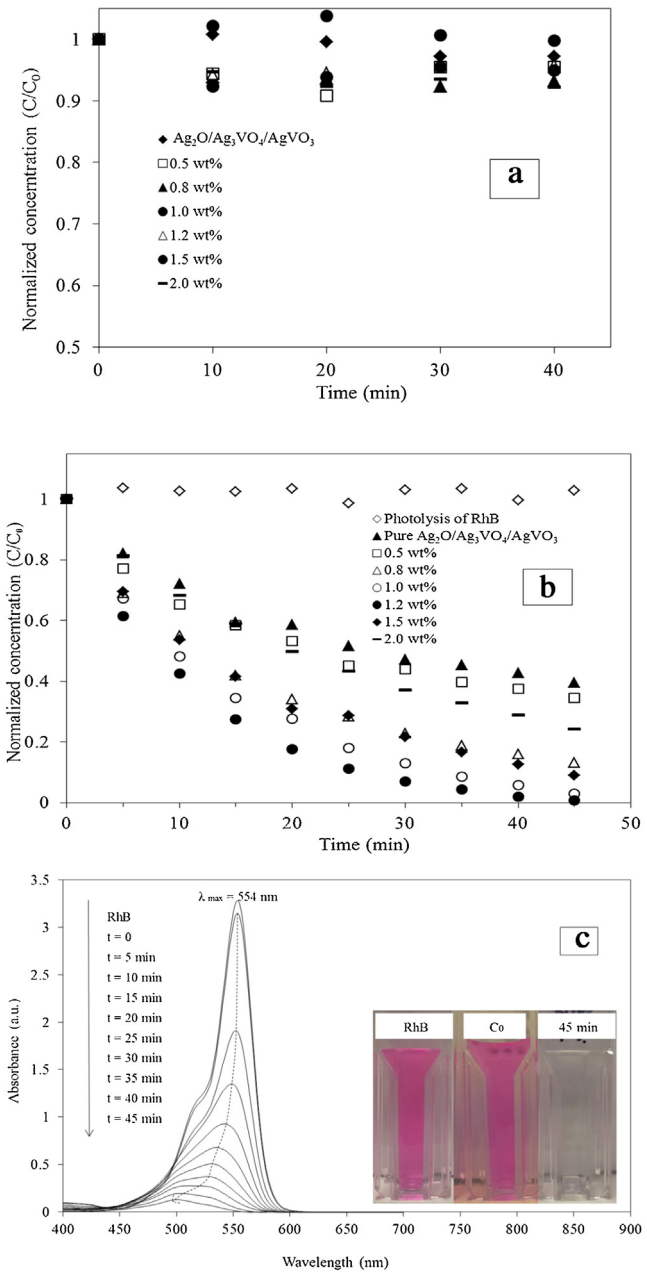

Fig. 8. (a): RhB adsorption by pure and GO-modified $Ag_2O/Ag_3VO_4/AgVO_3$ composites with various quantities of GO. (b): Photocatalytic RhB (15 mg L^{-1}) degradation by pure and GO-modified $Ag_2O/Ag_3VO_4/AgVO_3$ composites as well as RhB photolysis under VLI. (c) UV–vis spectra of reaction broth during RhB photocatalytic degradation by 1.2 wt% GO-modified $Ag_2O/Ag_3VO_4/AgVO_3$ composite.

peaks were identified as V^{5+}, corresponding well with the data from experiments involving KVO_3 [40].

Fig. 6c-i and c-ii show that the O 1s spectra observed were broad and deconvoluted into three separated peaks (dashed lines in Fig. 6c-i and c-ii), centered at 530.0 eV, 530.3 eV, and 531.4 eV as well as at 530.1 eV, 531.4 eV, and 533.1 eV for Fig. 6c-i and c-ii respectively. Of these six peaks, the peaks at 530.0 eV, 530.1 eV, 530.3 eV and 531.4 eV may be attributed to lattice oxygen in the heterogeneous multi-phase photocatalysts, while the observed peak of O 1s at 533.1 eV was ascribed to adsorbed oxygen [41].

Fig. 6d-i shows three types of observed carbon, centered at 285.0 eV (C—C), 286.4 eV (C—O), and 288.3 eV (C═O) [29]. It should be noted that the obtained C 1s spectra are attributed to the adsorbed carbon present in the as-prepared pure composite. While slightly different deconvolutions occurred in the C 1s spectrum of the 1.2 wt% GO-modified sample, Fig. 6d-ii shows three separated peaks centered at 285.0 eV (C—C), 286.9 eV (C—O), and 288.8 eV (O═C—O) [23]. Therefore, the chemical and electronic states of multi-phase GO-modified composites may be influenced by the addition of GO due to its electrical insulation via the disruption of sp^2 bonding networks [42].

3.5. Optical properties

In order to estimate the optical properties of the as-prepared fresh, multi-phase $Ag_2O/Ag_3VO_4/AgVO_3$ and GO-modified $Ag_2O/Ag_3VO_4/AgVO_3$ samples, UV–vis diffuse reflectance spectra were explored and the results are shown in Fig. 7. No significant differences in the UV–vis spectra of various samples were observed in Fig. 7, indicating that the addition of GO had little impact on the optical properties of as-prepared samples in the visible light region (380–750 nm), primarily due to the functionalized optical properties of GO shown in the UV light region (absorption peak of GO at 230 nm) [43], which had proved to be weak in the visible light region. Hence, the optical properties of GO-modified photocatalysts do not change substantially. In particular, the band gap energies of the as-synthesized fresh composites did not change substantially with the addition of GO. For this analysis, the band gap energies of the as-prepared composites were estimated using DRS results with the following formula:

$$\lambda = 1240/E_{bg} \quad (1)$$

where λ is the maximum wavelength of absorption by as-prepared samples (nm) (explained by the tangent dashed lines in Fig. 7), and E_{bg} is the estimated band gap energy of the samples (eV).

As shown in Fig. 7, ranges for the onset of visible light absorption by as-prepared samples were observed between 580 nm for pure $Ag_2O/Ag_3VO_4/AgVO_3$ and 565 nm for the 2.0 wt% GO-modified sample, resulting in 580 nm (0.0 wt%), 578 nm (0.5 wt%), 570 nm (0.8 wt%), 572 nm (1.0 wt%), 570 nm (1.2 wt%), 568 nm (1.5 wt%) and 565 nm (2.0 wt%), corresponding to calculated band gap energies of 2.14 eV, 2.15 eV, 2.18 eV, 2.17 eV, 2.18 eV, 2.18 eV and 2.19 eV respectively. Crucially, a calculated band gap energy of 2.18 eV was obtained for 1.2 wt% GO-modified samples shown by the center dashed line. Therefore, the band gap energies of as-synthesized samples were less influenced by the amount of added GO.

3.6. Photocatalytic degradation of organic dyes

3.6.1. Photodegradation of RhB

To quantify photocatalytic activity, RhB was used as a model organic pollutant under VLI, and the absorption spectra of RhB solution exposed to VLI were investigated over different periods of exposure. The corresponding results obtained are shown in Fig. 8a-c.

To achieve adsorption-desorption equilibrium, the adsorption reaction of RhB in the presence of various GO-modified silver species samples was performed over 40 min in the absence of light, the results of which are shown in Fig. 8a. It can be seen that adsorptions of 2.7%, 4.7%, 6.8%, 0.2%, 4.1%, 5% and 7.9% onto photocatalysts corresponding to $Ag_2O/Ag_3VO_4/AgVO_3$, as well as 0.5 wt%, 0.8 wt%, 1.0 wt%, 1.2 wt%, 1.5 wt% and 2.0 wt% GO-modified particles respectively.

As shown in Fig. 8b, compared to the pure multi-phase composite, samples containing GO exhibited higher photocatalytic activities towards the degradation of RhB. Of the GO-containing samples, 1.2 wt% GO-modified $Ag_2O/Ag_3VO_4/AgVO_3$ exhibited the highest photocatalytic activity, resulting in the photodegradation of 99.2% RhB in 45 min. This indicates that photocatalytic activity towards RhB degradation is proportional to the quantity of GO in the as-prepared samples. However, such photocatalytic activity was observed to decrease when the quantity of GO exceeded 1.2 wt%. As seen in Fig. 8b, the degradation of RhB using 1.5 wt% and 2.0 wt% GO samples was found to decrease, and the photocatalytic activities were similar to those which were seen in the 0.8 wt% and 0.5 wt% GO-modified composites, respectively.

As seen in Fig. 8c, the decline of RhB at the maximum absorption wavelength of 554 nm is primarily due to cleavage of the whole conjugated chromophore structure of RhB under VLI [44,45], with slightly progressive hypochromatic shifts of the absorption bands from 554 nm to 500 nm. This decomposition of RhB was verified by the change in colour of the RhB supernatant from pink to colourless, which occurred after 45 min, shown in the inset of Fig. 8c. Therefore, the high photocatalytic performance of GO-modified $Ag_2O/Ag_3VO_4/AgVO_3$ may be attributed to the synergistic effects of the adsorptivity of functionalized GO and multi-morphological features of heterogeneous photocatalysts.

3.6.2. Photodegradation of MO

To investigate the optimal GO-modified sample which exhibits a high photocatalytic performance towards the degradation of organic dyes under VLI, different types of dyes were applied to the degradation process. MO was used as a control to confirm that the photo-induced degradation process for different dyes was achieved using the 1.2 wt% GO-modified $Ag_2O/Ag_3VO_4/AgVO_3$ composite. Adsorption-desorption equilibrium of the photosystem was attained after 45 min in the absence of light followed by the light reaction, which is shown in Fig. 9a. The results of visible-light-induced photocatalytic performance towards the degradation of MO in both the absence and presence of photocatalysts are shown in Fig. 9b, and the absorption spectra of the MO aqueous solution under VLI for different time periods are shown in Fig. 9c.

To achieve adsorption-desorption equilibrium, the adsorption of MO in the presence of pure and 1.2 wt% GO-modified silver composites was performed over 40 min in the absence of light, the results of which are shown in Fig. 9a. It can be seen that adsorptions of 0.29% and 1.8% onto photocatalysts corresponded to $Ag_2O/Ag_3VO_4/AgVO_3$ and 1.2 wt% GO-modified particles, respectively.

A comparison of the performance of degradation of RhB and MO is shown in Figs 8 b and 9 b respectively. The concentration of MO was allowed to reach adsorption-desorption equilibrium in the absence of light over a period of 40 min. The photocatalytic activity towards the degradation of MO with pure $Ag_2O/Ag_3VO_4/AgVO_3$ decreased to 7% degradation under VLI over 45 min. However, 1.2 wt% GO-modified $Ag_2O/Ag_3VO_4/AgVO_3$ composite exhibited an enhanced photocatalytic performance with 92% degradation of MO under VLI over 45 min. As shown in Fig. 9c, the maximum light absorption of MO at a wavelength of 463 nm declined under VLI in the presence of 1.2 wt% GO-modified composite, suggesting that the chromophoric structure of MO had decomposed [46,47]. This

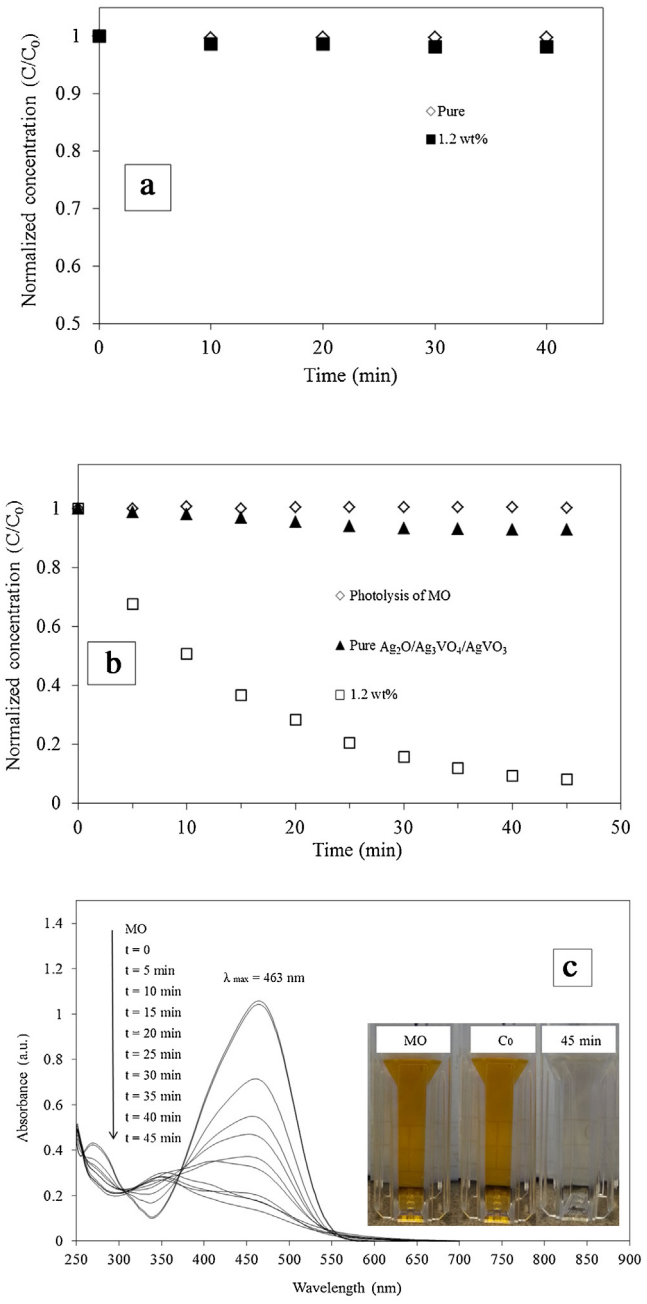

Fig. 9. (a): MO adsorption by pure and 1.2 wt% GO-modified $Ag_2O/Ag_3VO_4/AgVO_3$ composites. (b): Photocatalytic MO (15 mg L^{-1}) degradation by pure and 1.2 wt% GO-modified $Ag_2O/Ag_3VO_4/AgVO_3$ composites as well as MO photolysis under VLI. (c) UV–vis spectra of reaction broth during MO photocatalytic degradation by 1.2 wt% GO-modified $Ag_2O/Ag_3VO_4/AgVO_3$ composite.

decomposition of MO was verified by the colour change of the MO supernatant from yellow to colourless observed after 45 min, and is shown in the inset of Fig. 9c. Hence, the GO-modified multi-phase photocatalysts exhibited highly effective photocatalytic degradations of different dyes under VLI.

3.7. Stability of graphene oxide-$Ag_2O/Ag_3VO_4/AgVO_3$

To investigate the stabilities of multi-phase, pure and the multi-phase GO-modified $Ag_2O/Ag_3VO_4/Ag_4V_2O_7$ photocatalysts over the course of photocatalytic reactions, a number of characterization techniques and investigations were studied. The post-use characterization results are discussed in subsequent sections.

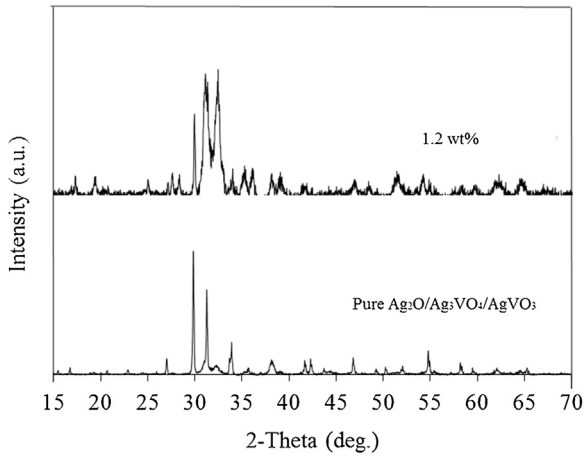

Fig. 10. XRD patterns of post-use pure and 1.2 wt% GO-modified $Ag_2O/Ag_3VO_4/AgVO_3$ composites.

3.7.1. Post-use XRD analysis

In order to further investigate changes to the crystal structures of multi-phase pure and GO-modified $Ag_2O/Ag_3VO_4/AgVO_3$ composites upon exposure to the photoactivity system, XRD analysis was performed on the recycled samples. The post-use patterns obtained for pure and 1.2 wt% GO-modified samples as representatives are shown in Fig. 10.

By comparing the corresponding fresh and post-use samples in Figs. 3 and 10 respectively, XRD patterns observed from the recovered post-use of pure $Ag_2O/Ag_3VO_4/AgVO_3$ and 1.2 wt% GO-modified samples showed different structural changes. As shown in Fig. 10, the declines of major peak intensities in the pure sample occurred at 30.96° and 32.42°, which is evident that the loss of crystallinity of α-Ag_3VO_4 occurred during the photocatalytic performance. Compared to the corresponding fresh sample, the major peak intensities of β-$AgVO_3$ and Ag_2O increased at 29.84° and 33.48°, as well as at 38.03° and 54.88° respectively, suggesting that the crystallinities of β-$AgVO_3$ and Ag_2O were increased in the photosystem due to photocorrosion of α-Ag_3VO_4 during photocatalytic operation. The reaction is shown in the following equation:

$$\alpha - Ag_3VO_4 \xrightarrow{VLI} \beta - AgVO_3 + Ag_2O \quad (2)$$

According to this hypothesis, XRD patterns from the post-use pure sample can be explained sensibly without suggesting the formation of new phases in the system. However, no changes of peak intensity were observed from the comparison with the fresh and post-use 1.2 wt% GO-modified samples, which can most likely be attributed to that the GO in the composites prevents the silver species from photocorrosion during photocatalytic reactions under VLI. These results agree well with reports that GO serves as a protective substrate which partially inhibits the photocorrosion of photocatalysts containing silver species [23,48].

3.7.2. Post-use SEM analysis

In order to explore the microstructure and morphology changes which occurred, the morphologies of the synthesized, multi-phase pure $Ag_2O/Ag_3VO_4/AgVO_3$ photocatalyst and the as-prepared composite in the presence of 1.2 wt% GO-modified were investigated by SEM after photocatalytic reactions. The images that were obtained are shown in Fig. 11.

SEM images from the recovered post-use of multi-phase pure $Ag_2O/Ag_3VO_4/AgVO_3$ and 1.2 wt% GO-modified samples showed different structural changes. Comparing Figs. 4 a and 11 a, dendritic-like plates disappeared while elongated, cylindrical-like structures and nanoparticles were formed after photocatalytic reactions

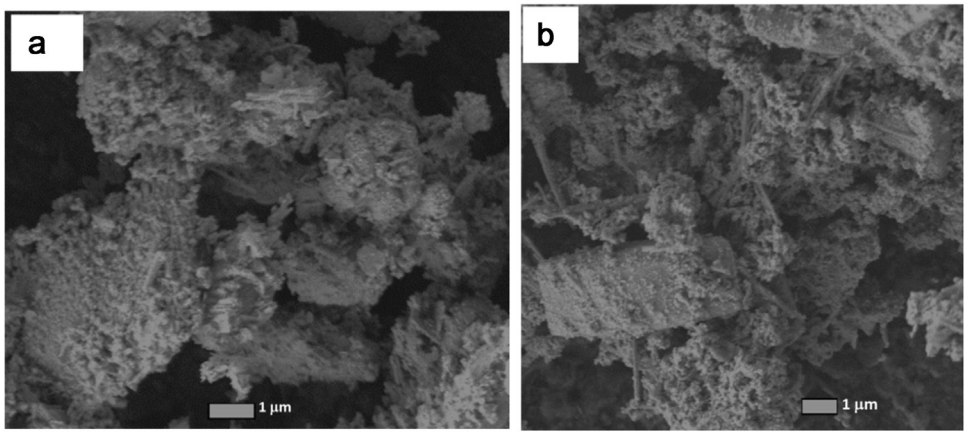

Fig. 11. SEM images of post-use composites. (a): pure $Ag_2O/Ag_3VO_4/AgVO_3$. (b): 1.2 wt% GO-modified $Ag_2O/Ag_3VO_4/AgVO_3$.

under VLI. In addition, crystals which were unobstructed by nanoscale granular particles before VLI were found to be completely encrusted by these cylindrical structures and nanoparticles after exposure to VLI, agreeing well with the post-use XRD results. However, no significant morphological changes were observed when comparing Figs. 11 b and 4 e, indicating that the photocatalytic performance towards the degradation of dyes was unable to strongly impact the morphologies of as-prepared GO-modified composites. This is most likely due to the use of GO as a modifier that contribute to the interactions among the species in the composite, which protects the multi-phase $Ag_2O/Ag_3VO_4/AgVO_3$ from photocorrosion under VLI. Therefore, the multi-morphological features of multi-phase composites could be partially maintained by GO to keep the photocatalytic activities of functionalized GO-modified photocatalysts high in regards to the degradation of organic dyes under VLI.

3.7.3. Post-use XPS analysis

In order to further investigate the chemical and electronic states of the post-use pure and 1.2 wt% GO-modified composites after photocatalytic reactions, XPS analysis was performed and the obtained results are shown in Fig. 12a-i. a-ii, b-i, b-ii, c-i and c-ii, as well as Fig. 12d-i and d-ii for Ag 3d, V 2p, O 1s and C 1s states, respectively. The binding energies obtained via XPS analysis were calibrated by referencing C 1s at 285 eV.

Comparing Ag 3d spectra in Figs. 6 and 12, the observed Ag 3d spectra of post-use samples had changed noticeably. The devolution which occurred in Ag 3d was assigned to two couples of peaks centered at 368.1 eV and 369.5 eV as well as at 374.1 eV and 375.6 eV (dashed lines in Fig. 12a-i), attributed to the binding energies of Ag $3d_{5/2}$ and Ag $3d_{3/2}$ respectively. Specifically, the peaks at 368.1 eV and 374.1 eV were ascribed to Ag^+, while the peaks at 369.5 eV and 375.6 eV were ascribed to Ag^0 [49]. However, no significant differences in the Ag 3d spectra were observed between Figs. 6 a-ii and 12 a-ii, indicating that two couples of peaks observed centered at 367.8 eV and 368.4 eV as well as at 373.8 eV and 374.4 eV (dashed lines in Fig. 12a-ii) were assigned to Ag $3d_{5/2}$ and Ag $3d_{3/2}$ orbits, respectively. Each of these peaks was ascribed to Ag^+, indicating that a minimal quantity of silver species was reduced to Ag^0 during photocatalytic performance in the form of dye degradation under VLI. Thus it is clear that GO, as the protective substrate, partially prevented the photocatalytic reduction of Ag^+ by transferring the photogenerated electrons from the silver species to the GO layer.

Comparing V 2p spectra in Figs. 6 and 12, some changes to V $2p_{3/2}$ and V $2p_{1/2}$ spectra which occurred in Fig. 12b-i were thought to be deconvoluted into three pairs of individual peaks centered at 516.5 eV/523.0 eV, 518.1 eV/523.9 eV, and 519.8 eV/525.3 eV (dashed lines in Fig. 12b-i), which correspond to V^{5+}. The shifts of peaks may be the result of changes to the states of vanadate ions in the crystal structures of multi-phase composites following photocatalytic performance. No differences in V 2p spectra were observed between Figs. 6 b-ii and 10 b-ii, indicating that the states of vanadate ions were stable in photocatalytic reactions under VLI, which agrees well with the XRD analyses of post-use samples.

In a comparison of O 1s and C 1s in Figs. 6 and 12, it was found that photocatalytic reactions also influence the chemical and electronic states of oxygen and carbon. As seen in Fig. 12c-i and c-ii, the observed deconvoluted peaks were centered at 532.0 eV and 532.5 eV, which are ascribed to oxide ions (e.g. O^{2-}), indicating that the states of oxygen species in composites changed following photocatalytic reactions. It might be because that the oxygen functional groups of the degradation intermediates or products adsorbed on the post-use photocatalysts. From Fig. 12d-i and d-ii, no major changes occurred in C 1s spectra compared to such spectra in fresh samples (Fig. 6d-i and d-ii). The peak at 289.0 eV, which was originally assigned to C═O shown in Fig. 6d-i, was assigned to be O═C—O after photocatalytic reactions. This was thought to be due to mineralized species generated from decomposed dye solutions which adsorbed to the post-use composites. Hence, GO could serve as a promising protective substrate to inhibit the photocorrosion of photocatalysts containing silver species in photosystems subject to VLI.

3.7.4. Post-use optical properties

Further investigation of the UV–vis diffuse reflectance spectra of post-use pure and 1.2 wt% GO-modified samples resulted in the intrinsic absorption under VLI shown in Fig. 13.

As shown in Fig. 13, no major differences in the intrinsic absorption were revealed in the post-use 1.2 wt% GO sample. However, a tail absorption peak at approximately 565 nm was observed in the absorption spectrum for the used, pure sample, which was ascribed to the increased generation of metallic silver (Ag^0) present in the composite without the addition of GO [50]. This indicates that Ag^+ ions may be reduced by accepting photogenerated electrons under VLI in the absence of sacrificial reagents [7] or modifiers. Therefore, comparison of the intrinsic absorption in the post-use samples after photocatalytic reactions under VLI showed that the GO-modified sample was more resistant to photocorrosion under VLI than the pure $Ag_2O/Ag_3VO_4/AgVO_3$ composite, which is in agreement with the XRD and SEM results shown in previous sections.

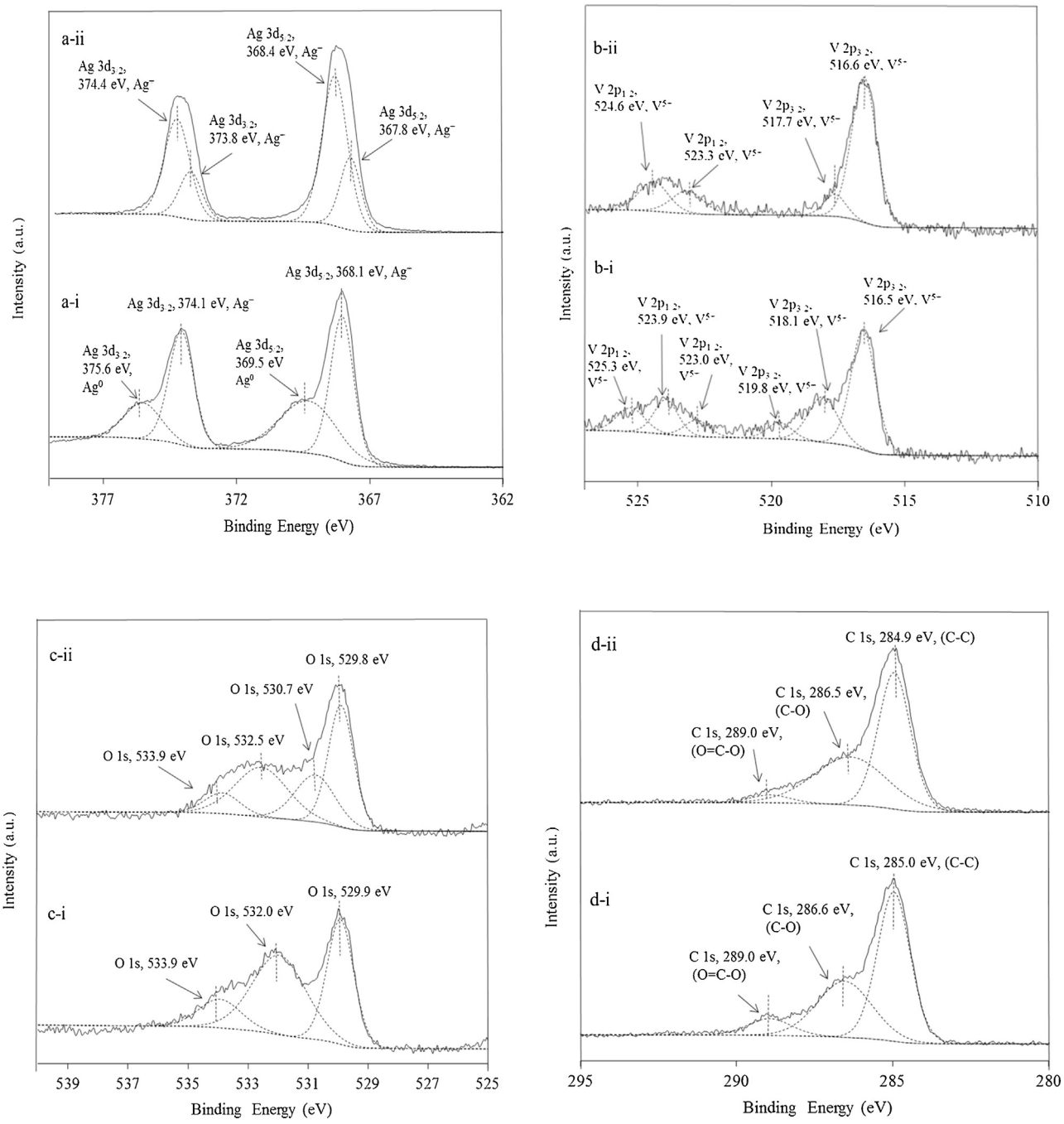

Fig. 12. High-resolution XPS spectra of post-use, pure (a-i, b-i, c-i and d-i) and 1.2 wt% GO-modified (a-ii, b-ii, c-ii and d-ii) $Ag_2O/Ag_3VO_4/AgVO_3$ composites. (a-i and a-ii): Ag 3d; (b-i and b-ii): V 2p; (c-i and c-ii): O1s; (d-i and d-ii): C 1s.

3.8. Role of reactive species testing in degradation of RhB and MO

In order to investigate the mechanism for the photocatalytic degradation of organic dyes, it is important to note that the role of the reactive species in photocatalysis serves as a significant clue towards unlocking the machinery of the photoactive performance, and must be explored. Quenching tests as diagnostic tools were therefore involved in the dye degradation studies. It is well known that reactive species such as holes (h^+), electrons (e^-), hydroxyl radicals ($^{\bullet}OH$) and superoxide radicals ($O_2^{\bullet-}$) play important roles in the photodegradation of organic pollutants [51–53]. Adsorption-desorption equilibrium of RhB and MO onto photocatalysts was achieved over 40 min in the absence of light, which was followed by the quenching tests using various reactive species scavengers (including BQ, AO and TBA) during the photodegradation of RhB and MO, the results of which are shown in Fig. 14a-d.

To achieve adsorption-desorption equilibrium, adsorption of RhB and MO in the presence of 1.2 wt% GO-modified $Ag_2O/Ag_3VO_4/AgVO_3$ composites were performed over 40 min in the absence of light, the results of which are shown in Fig. 14a and c respectively. This adsorption-desorption process resulted in the adsorptions of 4.1%, 4.6%, 7.1% and 3.6% onto photocatalysts shown in Fig. 14a, corresponding to a system without scavengers, as well as the scavengers of AO, BQ and TBA used in the quenching tests,

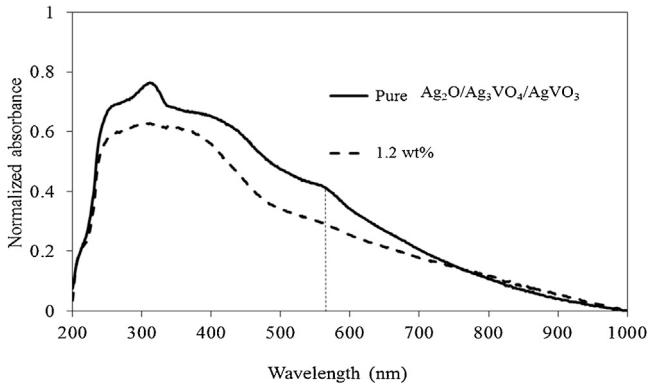

Fig. 13. UV–vis DRS of post-use pure and 1.2 wt% GO-modified $Ag_2O/Ag_3VO_4/AgVO_3$ composites.

respectively. As shown in Fig. 14c, the adsorption-desorption process also gave rise to the adsorptions of 1.8%, 2.6%, 2.4% and 1.6% onto photocatalysts shown in Fig. 14c, corresponding to a system without scavengers, as well as the scavengers of AO, BQ and TBA used in the quenching tests, respectively.

As shown in Fig. 14b, employing BQ as a scavenger for $O_2^{\bullet-}$ [54,55] successfully resulted in suppression of the degradation of RhB under VLI, reducing the degradation of RhB to 38% after 45 min. Using AO as a scavenger for h^+ [56,57] and TBA as a scavenger for $^{\bullet}OH$ [51] showed almost identical results in regards to the suppression of RhB degradation, both of which reduced the degradation of RhB to 89% after 45 min. In addition, as can be seen in Fig. 14d, BQ played a major role in the degradation mechanism for MO, reducing the degradation of MO to 6% after 45 min, and AO showed excellent suppression towards the degradation of MO as well with 19% MO degradation after 45 min. No major differences were observed following addition of TBA, indicating that $^{\bullet}OH$ is less likely to be restricted by TBA in the presence of MO in the photosystem. From these results, it can be concluded that oxygen plays a significant role in the photocatalytic oxidation of organic dyes (RhB and MO) on the surface of the GO-modified $Ag_2O/Ag_3VO_4/AgVO_3$ photocatalysts.

3.9. Mechanism of photocatalytic activity

The photodegradation pathways of the dyes (RhB and MO) in the presence of the 1.2 wt% GO-modified $Ag_2O/Ag_3VO_4/AgVO_3$ composite were investigated under VLI. Given the results obtained from the photolytic and photocatalytic degradation studies, as well as from the quenching tests, the possible reactions are proposed as follows:

$$Ag_2O + VLI \rightarrow Ag_2O(h^+ + e^-) \quad (3a)$$

$$Ag_3VO_4 + VLI \rightarrow Ag_3VO_4(h^+ + e^-) \quad (3b)$$

$$AgVO_3 + VLI \rightarrow AgVO_3(h^+ + e^-) \quad (3c)$$

$$h^+ + e^- \rightarrow \text{Heat} \quad (4)$$

$$AgVO_3(e^-) + GO \rightarrow AgVO_3 + GO_{(injected\ e^-)} \quad (5a)$$

$$GO_{(injectede^-)} + Ag_2O \rightarrow GO + Ag_2O_{(injected\ e^-)} \quad (5b\text{-}i)$$

$$GO_{(injectede^-)} + Ag_3VO_4 \rightarrow GO + Ag_3VO_{4(injected\ e^-)} \quad (5b\text{-}ii)$$

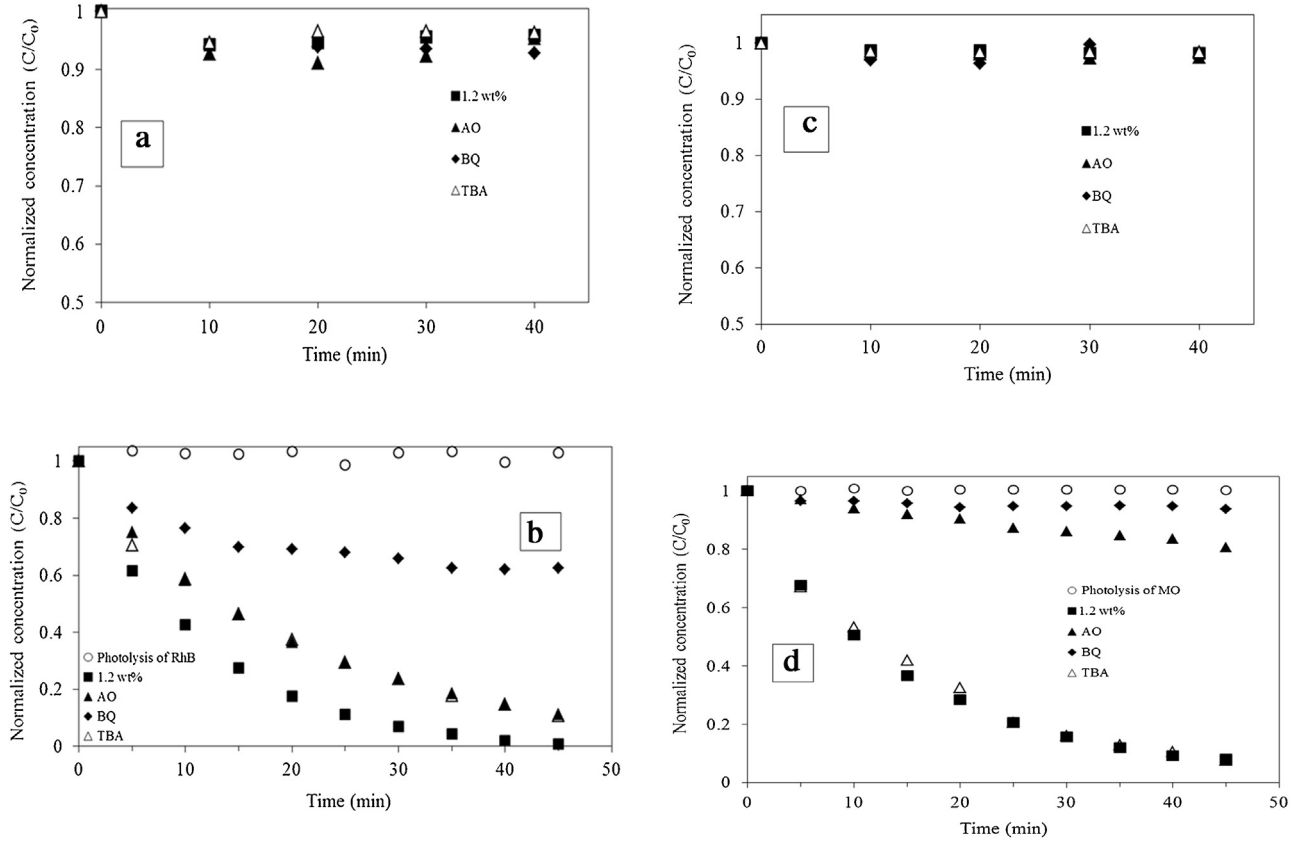

Fig. 14. (a): RhB adsorption by 1.2 wt% GO-modified $Ag_2O/Ag_3VO_4/AgVO_3$ composite, without (1.2 wt%) and with scavengers AO, BQ and TBA. (b): RhB profiles during RhB photocatalytic degradation by 1.2 wt% GO-modified $Ag_2O/Ag_3VO_4/AgVO_3$ under VLI, without (1.2 wt%) and with scavengers AO, BQ and TBA. (c): MO adsorption by 1.2 wt% GO-modified $Ag_2O/Ag_3VO_4/AgVO_3$ composite, without (1.2 wt%) and with scavengers AO, BQ and TBA. (d): MO profiles during MO photocatalytic degradation by 1.2 wt% GO-modified $Ag_2O/Ag_3VO_4/AgVO_3$ under VLI, without (1.2 wt%) and with scavengers AO, BQ and TBA.

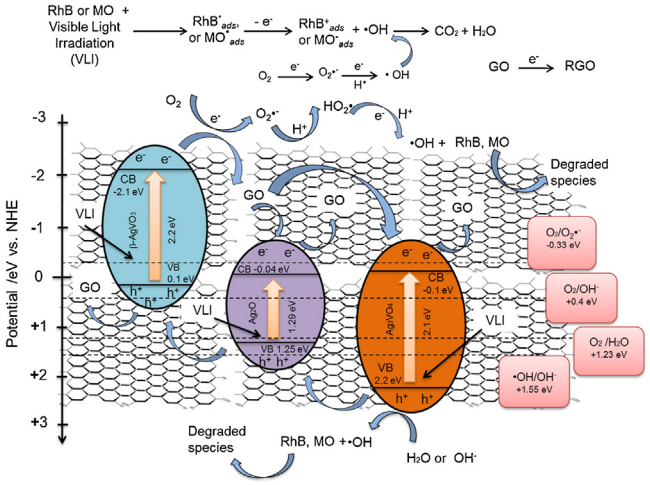

Fig. 15. Reaction mechanism of the photocatalytic degradation of organic dyes (RhB and MO) on 1.2 wt% GO-$Ag_2O/Ag_3VO_4/AgVO_3$ composite (white and hexagonal sheets represented GO in the diagram) under VLI.

$$AgVO_3(e^-) + Ag_2O \rightarrow AgVO_3 + Ag_2O_{(injected\ e^-)} \quad (5c\text{-}i)$$

$$AgVO_3(e^-) + Ag_3VO_4 \rightarrow AgVO_3 + Ag_3VO_{4(injected\ e^-)} \quad (5c\text{-}ii)$$

$$Ag_2O_{(injected\ e^-)} + GO \rightarrow Ag_2O + GO_{(injected\ e^-)} \quad (5d)$$

$$Ag_3VO_{4(injected\ e^-)} + GO \rightarrow Ag_3VO_4 + GO_{(injected\ e^-)} \quad (5e)$$

$$Ag_3VO_4(h^+) + Ag_2O \rightarrow Ag_3VO_4 + Ag_2O(h^+) \quad (6a)$$

$$Ag_2O(h^+) + AgVO_3 \rightarrow Ag_2O + AgVO_3(h^+) \quad (6b)$$

$$AgVO_3(h^+) + GO \rightarrow AgVO_3 + GO(h^+) \quad (6c)$$

$$e^-{}_{\text{on } AgVO_3 \text{ and GO)}} + O_2 \rightarrow O_2{}^{\bullet -} \quad (7a)$$

$$O_2{}^{\bullet -} + H^+ \rightarrow HO_2{}^{\bullet} \quad (7b)$$

$$HO_2{}^{\bullet} + 2e^- + H^+ \rightarrow {}^{\bullet}OH + OH^- \quad (7c)$$

$$GO_{(injected\ e^-)} + VLI \rightarrow RGO \quad (7d)$$

$$h^+ + H_2O \rightarrow {}^{\bullet}OH + H^+ \quad (8a)$$

$$4h^+ + 2H_2O \rightarrow 4H^+ + O_2 \quad (8b)$$

$$4h^+ + 2OH^- \rightarrow O_2 + 2H^+ \quad (8c)$$

$$RhB_{ads} \text{ or } MO_{ads} + VLI \rightarrow RhB^*{}_{ads} \text{ or } MO^*{}_{ads} \quad (9a)$$

$$RhB^*{}_{ads} \text{ or } MO^*{}_{ads} - e^- \rightarrow MO^+{}_{ads} \text{ or } RhB^+{}_{ads} + {}^{\bullet}OH \rightarrow \text{intermediates} \rightarrow CO_2 + H_2O [45, 52] \quad (9b)$$

The energy bands of Ag_2O, Ag_3VO_4 and $AgVO_3$ were identified using results reported in sources of literature [9,37,58]. As shown in Fig. 15, multi-phase heterogeneous $Ag_2O/Ag_3VO_4/AgVO_3$ particles are distributed on GO sheets, and the photocatalytic activity is initiated by the absorption of photons with wavelengths in the visible light region and energies larger than those of Ag_2O, Ag_3VO_4 and $AgVO_3$, corresponding to reactions (3a), (3b), and (3c) respectively.

In these reactions, the photogenerated e^--h^+ pairs form in the photocatalysts, then separate and move freely onto the surface of composites. That is to say that photo-excited electrons jump to the conduction band (CB) while holes remain on the valence band (VB), or are recombined as energy emissions under the internal electric field due to the characteristics of the components, in accordance with Reaction (4). Upon successful separation of the photo-excited e^--h^+ pair, a series of photocatalytic reactions occur in a particular sequence (from Reactions (5a), (5b-i), (5b-ii), (5c-i), (5c-ii), (5d), (5e), (9a) and (9b)). The distribution of Ag_2O, Ag_3VO_4 and $AgVO_3$ particles on GO sheets may be separated or intimate. For the separated Ag_2O, Ag_3VO_4 and $AgVO_3$ particles exposed to VLI, the photo-excited electrons on the CB of $AgVO_3$ are transferred to GO sheets which serve as bridges to facilitate interfacial charge transmission. As such, electrons are transferred to the CB of Ag_2O or Ag_3VO_4 along the GO sheets (Reactions (5a), (5b-i) and (5b-ii)). For the closely connected Ag_2O, Ag_3VO_4 and $AgVO_3$ particles exposed to VLI, the photogenerated electrons are directly transferred from the CB of $AgVO_3$ to those of Ag_2O and Ag_3VO_4 (Reactions (5c-i) and (5c-ii)).

The photo-excited electrons on the CBs of Ag_2O and Ag_3VO_4 are next transferred to GO sheets (Reactions (5d) and (5e)). This step serves as an alternative to the accumulation of electrons in the conduction bands which results in the photocorrosion of Ag^+ in silver species composites, or to being trapped by adsorbed molecular oxygen (O_2) due to the increased positive CB potentials of Ag_2O and Ag_3VO_4 relative to the standard redox potential of $O_2/O_2{}^{\bullet -}$ (-0.33 eV vs. NHE). These electrons which are transferred to GO sheets are trapped by the adsorbed O_2 on the photocatalysts to eventually produce $O_2{}^{\bullet -}$. The photo-excited electrons left on the CB of $AgVO_3$ are also captured by adsorbed O_2 to produce $O_2{}^{\bullet -}$. Subsequently, hydroxyl radicals ($^{\bullet}OH$) are eventually generated after a series of reactions with the photo-excited electrons and protons (H^+), in accordance with reactions (7a), (7b) and (7c) [59]. The generated $O_2{}^{\bullet -}$ was confirmed to be the key reactive species, playing a significant role in the degradation of organic dyes (RhB and MO) under VLI. In addition, GO sheets with an excess of electrons could be reduced to RGO under VLI (reaction (7d)), indicating that GO as the protective substrate may be employed to avoid photocorrosion in heterogeneous $Ag_2O/Ag_3VO_4/AgVO_3$ composites [23,48].

Holes on the VB of Ag_3VO_4 can be trapped by adsorbed H_2O or OH^- ions formed from the hydrolysis of H_2O on the surface of photocatalysts, yielding $^{\bullet}OH$, H^+ and O_2 in accordance with reactions (8a), (8b) and (8a). Holes on the VB of Ag_2O can react with H_2O and OH^- giving rise to reactions (8b) and (8c), according to the internal electric field that is present. Moreover, the transfer of holes from the VB of Ag_3VO_4 to that of Ag_2O, and then to that of $AgVO_3$ is enhanced with the modification of GO sheets. The photo-excited holes transferred to the VB of $AgVO_3$ are shifted to GO sheets rather than captured by the adsorbed H_2O and OH^- ions on the surface to give $^{\bullet}OH$, H^+ and O_2, due to the increased negative potential of the VB of $AgVO_3$ with respect to the standard redox potentials of $^{\bullet}OH/OH^-$ (1.55 eV vs. NHE) (reaction (8a)), O_2/H_2O (1.23 eV vs. NHE) (Reaction (8b)) and O_2/OH^- (0.4 eV vs. NHE) (Reaction (8c)) [60]. Subsequently, holes shifted to GO sheets may eventually react with the reactive species.

During the overall photocatalytic degradation process, photogenerated electrons play a key role in the production of $O_2{}^{\bullet -}$ radicals, resulting in the generation of strong $^{\bullet}OH$ radicals. These subsequently give rise to the direct oxidization of RhB and MO (Reactions (9a) and (9b)) [61] on the surface of GO-modified $Ag_2O/Ag_3VO_4/AgVO_3$ composites. Therefore, functional GO sheets facilitate the separation of photogenerated e^--h^+ pairs by shifting the charges in order to inhibit the recombination of e^--h^+ pairs. Electrons transferred from the silver species to the GO sheets resulted in the prevention of silver ions being reduced to metallic silver. In turn, this allows GO sheets to be intimately involved in the complete photocatalytic reaction series describing the degradation of organic pollutants (RhB and MO) under VLI, resulting in an enhanced photocatalytic performance.

4. Conclusions

Novel multi-phase $Ag_2O/Ag_3VO_4/AgVO_3$ photocatalysts in the presence of various quantities of GO were synthesized using a facile method at room temperature. Characterization results indicated that observable changes in multi-morphological features occurred in the multi-phase composites, and that photocorrosion of silver species was partially inhibited with the addition of GO. The high photocatalytic activity with regards to the decomposition of organic dyes under VLI may be attributed to the synergistic effects between the absorbability of functionalized GO, its interactions with other species in the composite during photocatalytic reactions, and the multi-morphological features of heterogeneous photocatalysts. The quantity of GO in the photocatalysts worked in conjunction with the crystallinity of crystal structures and morphologies to increase photocatalytic efficiency. In addition, the optimum quantity of GO was investigated and determined to be 1.2 wt% combined with high-crystallinity heterogeneous $Ag_2O/Ag_3VO_4/AgVO_3$ composites. This gave rise to the optimal photocatalytic performance with regards to the degradation of organic dyes, demonstrating 99.2% degradation of RhB and 92% degradation of MO after 45 min under VLI. This study may provide a new photocatalytic perspective on the facilitation of the practical applications of photocatalysts in environmental issues.

Acknowledgments

This work was funded by the Natural Sciences and Engineering Research Council of Canada (NSERC). The authors would like to thank Dr. Alexander Mommers and Dr. Yun Liu at the Center for Catalysis Research and Innovation, and the Department of Earth Sciences at the University of Ottawa, as well as Dr. Jianqun Wang at Carleton University for their helps in sample characterizations. The authors would also like to thank China Scholarship Council for the scholarships to Dr. Rong Ran and Mr. Xiangchao Meng during the study.

References

[1] A. Kudo, Y. Miseki, Chem. Soc. Rev. 38 (2009) 253–278.
[2] A.J. Nozik, R. Memming, J. Phys. Chem. 100 (1996) 13061–13078.
[3] M.G. Walter, E.L. Warren, J.R. McKone, S.W. Boettcher, Q. Mi, E.A. Santori, N.S. Lewis, Chem. Rev. 110 (2010) 6446–6473.
[4] R. Konta, H. Kato, H. Kobayashi, A. Kudo, Phys. Chem. Chem. Phys. 5 (2003) 3061–3065.
[5] X. Tao, Q. Hong, T. Xu, F. Liao, J. Mater. Sci. Mater. Electron. 25 (2014) 3480–3485.
[6] X. Lin, J. Xing, W. Wang, Z. Shan, F. Xu, F. Huang, J. Phys. Chem. C 111 (2007) 18288–18293.
[7] P. Dong, Y. Wang, B. Cao, S. Xin, L. Guo, J. Zhang, F. Li, Appl. Catal. B 132–133 (2013) 45–53.
[8] Y. Bi, S. Ouyang, J. Cao, J. Ye, Phys. Chem. Chem. Phys. 13 (2011) 10071–10075.
[9] W. Jiang, X. Wang, Z. Wu, X. Yue, S. Yuan, H. Lu, B. Liang, Ind. Eng. Chem. Res. 54 (2015) 832–841.
[10] G. Dai, J. Yu, G. Liu, J. Phys. Chem. C 116 (2012) 15519–15524.
[11] C. Belver, C. Adán, S. García-Rodríguez, M. Fernández-García, Chem. Eng. J. 224 (2013) 24–31.
[12] C. Yu, G. Li, S. Kumar, K. Yang, R. Jin, Adv. Mater. 26 (2014) 892–898.
[13] C. Yu, L. Wei, W. Zhou, J. Chen, Q. Fan, H. Liu, Appl. Surf. Sci. 319 (2014) 312–318.
[14] C. Yu, L. Wei, J. Chen, Y. Xie, W. Zhou, Q. Fan, Ind. Eng. Chem. Res. 53 (2014) 5759–5766.
[15] J. Li, W. Fang, C. Yu, W. Zhou, L. Zhu, Y. Xie, Appl. Surf. Sci. 358 (Part A) (2015) 46–56.
[16] D.R. Dreyer, S. Park, C.W. Bielawski, R.S. Ruoff, Chem. Soc. Rev. 39 (2010) 228–240.
[17] V. Singh, D. Joung, L. Zhai, S. Das, S.I. Khondaker, S. Seal, Prog. Mater Sci. 56 (2011) 1178–1271.
[18] Q. Xiang, J. Yu, M. Jaroniec, Chem. Soc. Rev. 41 (2012) 782–796.
[19] J. Li, L. Wei, C. Yu, W. Fang, Y. Xie, W. Zhou, L. Zhu, Appl. Surf. Sci. 358 (Part A) (2015) 168–174.
[20] Z. Ji, X. Shen, J. Yang, Y. Xu, G. Zhu, K. Chen, Eur. J. Inorg. Chem. 2013 (2013) 6119–6125.
[21] Q. Liang, Y. Shi, W. Ma, Z. Li, X. Yang, Phys. Chem. Chem. Phys. 14 (2012) 15657–15665.
[22] Y. Ao, P. Wang, C. Wang, J. Hou, J. Qian, Appl. Surf. Sci. 271 (2013) 265–270.
[23] C. Dong, K.L. Wu, X.W. Wei, X.Z. Li, L. Liu, T.H. Ding, J. Wang, Y. Ye, CrystEngComm 16 (2014) 730–736.
[24] Y. Song, J. Zhu, H. Xu, C. Wang, Y. Xu, H. Ji, K. Wang, Q. Zhang, H. Li, J. Alloys Compd. 592 (2014) 258–265.
[25] M. Zhu, P. Chen, M. Liu, ACS Nano 5 (2011) 4529–4536.
[26] M. Zhu, P. Chen, M. Liu, Langmuir 28 (2012) 3385–3390.
[27] B.F. Machado, P. Serp, Catal. Sci. Technol. 2 (2012) 54–75.
[28] L. Han, P. Wang, S. Dong, Nanoscale 4 (2012) 5814–5825.
[29] H. Zhang, X. Fan, X. Quan, S. Chen, H. Yu, Environ. Sci. Technol. 45 (2011) 5731–5736.
[30] G.T. Pan, M.H. Lai, R.C. Juang, T.W. Chung, T.C.K. Yang, Ind. Eng. Chem. Res. 50 (2011) 2807–2814.
[31] Q. Yu, Z.R. Tang, Y.J. Xu, J. Energy Chem. 23 (2014) 564–574.
[32] W. Zhou, H. Liu, J. Wang, D. Liu, G. Du, J. Cui, ACS Appl. Mater. Interfaces 2 (2010) 2385–2392.
[33] B. Yao, M. Liu, Z. Ma, C. Wang, Adv. Mater. Res. 148–149 (2011) 1331–1338.
[34] J. Zhou, G. Tian, Y. Chen, Y. Shi, C. Tian, K. Pan, H. Fu, Sci. Rep. 4 (2014) 4027.
[35] R.E. Dinnebier, A. Kowalevsky, H. Reichert, M. Jansen, Zeitschrift für Kristallographie-cryst Mater. 222 (2007) 420–426.
[36] C.M. Huang, G.T. Pan, Y.C.M. Li, M.H. Li, T.C.K. Yang, Appl. Catal. A 358 (2009) 164–172.
[37] H. Shi, C. Zhou, C. Zhang, Res. Chem. Intermed. (2014) 1–13.
[38] K.S. Raju, M.K. Pour Seydei, S.A. Suthanthiraraj, Mater. Lett. 19 (1994) 65–68.
[39] W.S. Wang, H. Du, R.X. Wang, T. Wen, A.W. Xu, Nanoscale 5 (2013) 3315–3321.
[40] D. Courcot, A. Ponchel, B. Grzybowska, Y. Barbaux, M. Rigole, M. Guelton, J.P. Bonnelle, Catal. Today 33 (1997) 109–118.
[41] Z. Sun, J. Guo, S. Zhu, L. Mao, J. Ma, D. Zhang, Nanoscale 6 (2014) 2186–2193.
[42] D. Krishnan, F. Kim, J. Luo, R. Cruz-Silva, L.J. Cote, H.D. Jang, J. Huang, Nano Today 7 (2012) 137–152.
[43] E.Y. Choi, T.H. Han, J. Hong, J.E. Kim, S.H. Lee, H.W. Kim, S.O. Kim, J. Mater. Chem. 20 (2010) 1907–1912.
[44] Z. He, C. Sun, S. Yang, Y. Ding, H. He, Z. Wang, J. Hazard. Mater. 162 (2009) 1477–1486.
[45] T. Wu, G. Liu, J. Zhao, H. Hidaka, N. Serpone, J. Phys. Chem. B 102 (1998) 5845–5851.
[46] R. Zha, R. Nadimicherla, X. Guo, J. Mater. Chem. A 3 (2015) 6565–6574.
[47] Z. Wang, L. Yin, Z. Chen, G. Zhou, H. Shi, J. Nanomater. 2014 (2014) 6.
[48] M. Cao, P. Wang, Y. Ao, C. Wang, J. Hou, J. Qian, Int. J. Hydrogen Energy 40 (2015) 1016–1025.
[49] M.S.A.S. Shah, M. Nag, T. Kalagara, S. Singh, S.V. Manorama, Chem. Mater. 20 (2008) 2455–2460.
[50] G. Li, K.H. Wong, X. Zhang, C. Hu, J.C. Yu, R.C.Y. Chan, P.K. Wong, Chemosphere 76 (2009) 1185–1191.
[51] J. Wang, X. Yang, J. Chen, J. Xian, S. Meng, Y. Zheng, Y. Shao, D. Li, J. Am. Ceram. Soc. 97 (2014) 267–274.
[52] J. Zhao, C. Chen, W. Ma, Top. Catal. 35 (2005) 269–278.
[53] J. Wang, P. Wang, Y. Cao, J. Chen, W. Li, Y. Shao, Y. Zheng, D. Li, Appl. Catal. B 136–137 (2013) 94–102.
[54] M. Stylidi, D.I. Kondarides, X.E. Verykios, Appl. Catal. B 47 (2004) 189–201.
[55] P. Raja, A. Bozzi, H. Mansilla, J. Kiwi, J. Photochem. Photobiol. A 169 (2005) 271–278.
[56] H. Lin, H. Ye, S. Chen, Y. Chen, RSC Adv. 4 (2014) 10968–10974.
[57] W. Li, D. Li, W. Zhang, Y. Hu, Y. He, X. Fu, J. Phys. Chem. C 114 (2010) 2154–2159.
[58] G. Trimarchi, H. Peng, J. Im, A.J. Freeman, V. Cloet, A. Raw, K.R. Poeppelmeier, K. Biswas, S. Lany, A. Zunger, Phys. Rev. B 84 (2011) 165116.
[59] S. Horikoshi, H. Hidaka, N. Serpone, Environ. Sci. Technol. 36 (2002) 1357–1366.
[60] A.J. Bard, R. Parsons, J. Jordan, Marcel Dekker: New York (1985).
[61] Q. Zhu, W.S. Wang, L. Lin, G.Q. Gao, H.L. Guo, H. Du, A.W. Xu, J. Phys. Chem. C 117 (2013) 5894–5900.